

Investigating the Role of Gravity Waves on Mesosphere-Lower-Thermosphere

(MLT) Inversions at Low Latitudes

Chalachew Lingerew^{1*}, U. Jaya Prakash Raju¹

¹ Department of Physics, Washera Geospace, and Radar Science Laboratory, Bahir Dar University, Bahir Dar, Ethiopia

Correspondence to: Chalachew Lingerew Bizuneh (chalachewlingerew@gmail.com)

Abstract

The Mesosphere and Lower-Thermosphere (MLT) transitional region, encompassing a height range of 60-100 km, is a distinct and highly turbulent zone within the Earth's atmosphere. The region is significant owing to dynamics of atmospheric processes like planetary, tidal, and particularly gravity waves, which contribute to the formation of the Mesospheric Inversion Layer (MIL). Investigating the inversion phenomena is crucial for understanding the dynamics of the middle and upper atmosphere, especially regarding stability and energy transfer. These phenomena are associated with energy transfer processes, vital for understanding the overall dynamics of the atmosphere. Despite extensive study on an inversion, the formation mechanisms of mesospheric inversions remain poorly understood. Hereunder, the upper and lower inversion phenomena and their causative mechanisms are explored. It utilizes long-term SABER observations during 2005-2020 over the latitude, 3-15° N and longitude, 33-48° E ranges. The results show that the upper inversion occurs more frequently, with a frequency below 40%, compared to the lower inversion, which occurs below 20%. The upper inversion occurs within the height range of 78-91 km, with an inversion amplitude of approximately 20-80 K and a thickness of around 3-12 km. In contrast, the lower inversion is confined to the height range of 70-80 km, with an inversion amplitude of about 10-60 K and a thickness of around 4-10 km. Moreover, the gravity wave indicator potential energy shows high energy (below 100 J/kg) in the upper MLT region (85-90 km) compared to the lower MLT region (70-75 km) with less than 50 J/kg. Considering gravity waves, the Brunt-Väisälä frequency (N^2) stability criteria indicate instability in the upper MLT region with very low values compared to the lower MLT region. This suggests that the high amount of gravity wave potential energy is a consequence of the higher instability in the upper inversion compared to the lower inversion.

Keywords: Mesosphere and Lower Thermosphere (MLT), Upper and Lower Inversions, Perturbed Temperature, Causative Gravity Waves, Potential Energy, Brunt-Väisälä Frequency, Atmospheric Instability.

33 Introduction

34 The Mesosphere and Lower-Thermosphere (MLT) region serves as a transitional zone for
35 atmospheric wave processes from the lower and upper atmospheres, including tidal, planetary,
36 and gravity waves. Gravity waves (GWs) originating in the lower atmosphere propagate into the
37 upper mesosphere, where they break and dissipate, releasing energy and momentum. This
38 process influences the thermal structure, global atmospheric circulation, and mesospheric
39 inversion layers (MILs), which are associated with increased temperature variability in
40 mesosphere. MILs indicate wave saturation when the lapse rate falls below the dry adiabatic
41 lapse rate (Sica et al., 2007). Temperature inversions in the mesosphere have been widely
42 observed and studied using various techniques, including lidar, radar, rocket sondes, and
43 satellites, across different geographic locations. Sivakandan et al. (2014) utilized
44 TIMED/SABER kinetic temperature data to examine the occurrence and characteristics of
45 mesospheric inversions over the equatorial Indian region (0 to 10° N and 70 to 90° E) for the
46 years 2002 and 2008. However, they did not explore the causative factors. This study aims to
47 investigate the causes of these inversions, focusing specifically on the role of atmospheric
48 gravity waves.

49 Gravity waves and mesospheric inversion layers (MILs) are interconnected phenomena within
50 the Earth's atmosphere, particularly in the mesosphere and lower thermosphere (MLT).
51 Inversions are layers within the mesosphere where the temperature profile exhibits an increment.
52 As a result, the temperature increases with altitude, contrary to the typical decrease. These
53 inversion layers often form because of this atmospheric wave dynamic processes, including the
54 breaking and dissipation of gravity waves. As gravity waves propagate upwards, they can grow
55 in amplitude since the atmospheric density decreases with altitude. While these waves reach a
56 critical amplitude, they become broken. This breaking process releases energy and momentum
57 into the surrounding atmosphere, leading to localized heating that creates or enhances
58 mesospheric inversion layers by increasing the temperature with altitude. The breaking of gravity
59 waves contributes to momentum and energy deposition can also generate turbulence, which
60 further influences the structure and instability of an inversion layers.

61 The deposition of momentum and energy from gravity waves (GWs) is considered a major factor
62 driving large-scale atmospheric circulation, the coupling between atmospheric layers, and the
63 occurrence of inversion phenomena (Fritts and Alexander, 2003; Lindzen, 1981; Smith, 2012).
64 Researchers are also investigating the effects of gravity wave breaking on MLT dynamics to

65 better understand its role in inversion phenomena, especially in mid- and high-latitude regions
66 (Gan et al., 2012; Walterscheid and Hickey, 2009; Collins et al., 2011; Szewczyk et al., 2013).
67 Observational and modeling studies have examined gravity waves (GWs) as a contributing factor
68 to these inversions (Fritts, 2018; Collins et al., 2014; Sridharan et al., 2008; Ramesh and
69 Sridharan, 2012; Ramesh et al., 2013, 2014, 2017). Despite extensive research, our
70 understanding of how gravity waves influence mesosphere inversions-particularly regarding
71 temperature variability-remains incomplete, even in mid- and high-latitude regions (Singh and
72 Pallamraju, 2018; Fritts et al., 2018). **Consequently, studying inversion phenomena and their**
73 **underlying causes continues to be a crucial area of investigation, especially within MLT**
74 **dynamics over low-latitude.**
75 **Research on the temporal and spatial variability of the mesosphere inversion phenomenon,**
76 **regarding atmospheric waves, particularly gravity wave activity, is notably lacking in low**
77 **latitudes.** To address this gap, our study investigates the mesosphere inversion phenomenon and
78 its association with gravity wave activity and instability criteria. We use Brunt-Vaisala frequency
79 (N^2) over the low latitudinal band (3° – 15° N) with long-term SABER observations from 2005 to
80 2020. The study is organized as follows: Section 2 details the data and methodology used to
81 analyze the mesosphere inversion phenomenon and their causative gravity waves via the
82 potential energy. Section 3 presents the results, and Section 4 concludes the findings.

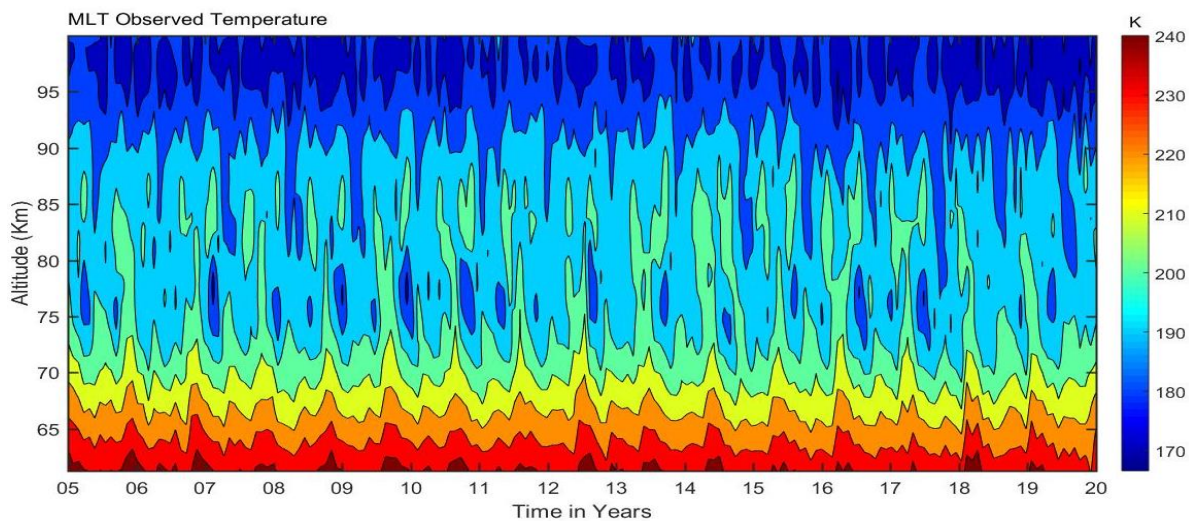
83 **2. Observation and Data analysis**

84 **2.1 SABER Observation**

85 The TIMED/SABER satellite, launched on December 7, 2001, operates in an elliptical orbit at
86 approximately 625 km altitude with a 74° inclination relative to the equator. Since its launch,
87 SABER has been a crucial tool for atmospheric research, providing extensive data on the middle
88 and upper atmosphere. SABER is a limb-viewing radiometer working in the infrared region
89 (1.27–17 microns) and can measure radiative emissions across a wide range of altitudes. It offers
90 nearly global coverage and continuous 24-hour data over 60 days. The instrument completes 15
91 orbits daily, each taking about 97 minutes, and collects around 1400 data files per day, with each
92 profile taking 58 seconds. SABER's high-resolution temperature profiles are essential for
93 studying the dynamics and wave processes in the MLT. It provides temperature measurements
94 with an accuracy of 1 to 2 K between 15 and 60 km. The accuracy decreases to 5 K below 85 km
95 and increases to 6.7 K to 10 K near 100 km. This data has been crucial in enhancing our
96 understanding of the thermal structure and dynamic processes in the mesospheric region, as

97 emphasized by several studies (Garcia et al., 2008; Gan et al., 2012, 2014; Bizuneh et al., 2022;
98 Lingerew et al., 2023; Rezac et al., 2015; Meriwether and Gerrard, 2004; Fechine et al., 2008;
99 Dou et al., 2009; France et al., 2015).

100 Owing to this, we used the SABER vertical temperature profiles collected within the 60–100 km
101 altitude range. These profiles encompass the period from 2005 to 2020, covering latitudes from
102 3°N to 15°N and longitudes from 33°E to 48°E. Figure 1 illustrates the monthly mean SABER
103 temperature data for the mesosphere and lower thermosphere. The data aim to illustrate the MLT
104 temperature variability, which helps us identify the inversion layers (MIL). The monthly mean
105 temperatures in the MLT region show a maximum of 200-240 K at altitudes of 60-70 km. Then it
106 decreases to around 160-180 K at 95-100 km throughout the entire period. While the temperature
107 patterns in the 70-90 km altitude range suggest an inversion, these inversions are not visible.



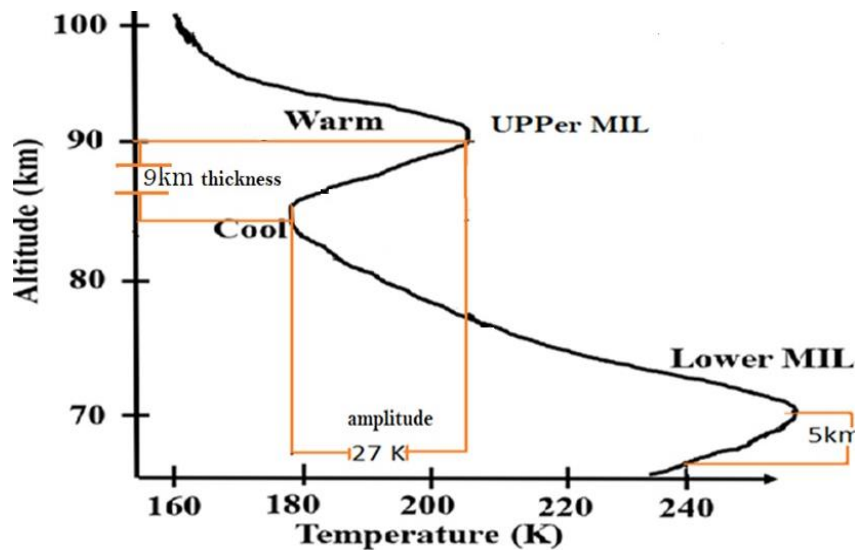
108 **Figure 1.** The monthly mean of MLT temperature variability in the height range of 60-100 km
109 during 2005-2020 over the low-latitude.
110

111 2.2 Analysis Technique

112 The Earth's middle atmosphere typically has a negative temperature gradient, but some reports
113 have shown positive temperature gradients in the mesosphere (Meriwether and Gardner, 2000;
114 Gan et al., 2012). This phenomenon, known as the "mesospheric inversion layer (MIL)," is
115 identified using the method described by Leblanc and Hauchecorne (1997) and Fechine et al.
116 (2008). Mesospheric inversions are defined by their thickness (the altitude difference between
117 the maximum warming and cooling) and their amplitude (the temperature difference between

118 these points) (Meriwether and Gardner, 2000). The following are the criteria for identifying these
119 inversions:

- 120 1. The bottom level of the lower inversion is above 70 km, and the top level is below 80 km.
121 For the upper inversion, the bottom level is above 80 km, and the top level is below 92
122 km.
- 123 2. The amplitude is considered larger than 5 K.
- 124 3. The thickness is greater than or equal to 3 km.



125
126 Figure 2. Schematic of upper and lower mesospheric inversion layers shown in the temperature
127 profile for the MLT regions (Adapted from Meriwether and Gerrard, 2004).

128 Figure 2 illustrates this concept, highlighting the positive temperature difference between the top
129 and bottom levels of the inversion. This method has been widely applied in numerous studies
130 investigating mesospheric inversions (Leblanc et al., 1998; Meriwether and Gardner, 2000; Duck
131 et al., 2001; Duck and Greene, 2004; Cutler et al., 2001; Siva Kumar et al., 2001; Ratnam et al.,
132 2003; Gan et al., 2012). In addition, the frequency of mesospheric inversion layer (MIL)
133 occurrences is determined for the period 2005–2020 in both the upper and lower MLT regions.
134 This frequency is calculated by dividing the number of inversion days in each month by the total
135 number of days in that month over the 16-year observation period (2005–2020).

136 Mesospheric temperature inversions are linked to MLT instabilities driven by the dynamics of
137 atmospheric wave processes. To identify the causative, short-period atmospheric gravity waves,
138 a high-pass filter with a one-hour interval cutoff frequency is applied using the Brunt-Väisälä

139 frequency (N²). Another important concept to estimate the Brunt-Vaisala frequency is the
 140 potential temperature (θ). It represents the air parcel's temperature when it is displaced
 141 adiabatically to a standard pressure level, p_0 , from the current pressure level, p . This is based on
 142 the first law of thermodynamics.

$$143 \quad \frac{dT}{T} = \frac{R}{c_p} \frac{dp}{p} \Rightarrow \int_T^0 \frac{dT}{T} = \int_p^{p_0} \frac{R}{c_p} \frac{dp}{p} \quad (1) \text{ it yields}$$

$$144 \quad \theta = T \left(\frac{p_0}{p} \right)^{R/c_p} \quad (2)$$

145 The vertical motion of an atmospheric air parcel can thus be described by (Liu, 2011; Vadas and
 146 Fritts, 2005) as shown in equation (2). This equation calculates the Brunt-Väisälä frequency of
 147 the parcel, accounting for the buoyant and gravitational forces acting upon it.

$$148 \quad \frac{d^2s}{dt^2} = -g \frac{\rho - \rho_0}{\rho} \sin a \quad (3)$$

149 Based on the hydrostatic equation, $\rho = \rho_0$, and $p = p_0 \Rightarrow \frac{\partial p}{\partial z} = \frac{\partial p_0}{\partial z} = -g\rho_0$ (4) and the ideal gas
 150 law, $\rho = p/RT = p_0/RT$ gives the parcels motion of an equation:

$$151 \quad \frac{d^2s}{dt^2} = -\frac{g}{\rho} \left(\frac{d\rho}{dp} \frac{\partial p_0}{\partial z} - \frac{\partial \rho_0}{\partial z} \right) z \quad (5)$$

152 Following the same approach using the hydrostatic equation (4) and adiabatic equation (6)

$$153 \quad d \ln p = \frac{d \ln p}{\gamma}, \gamma = c_p/c_v \quad (6) \text{ yields}$$

$$154 \quad \frac{d^2s}{dt^2} = -\frac{g}{\rho} \left(\frac{\rho}{\gamma p_0} \frac{\partial p_0}{\partial z} - \frac{\partial \rho_0}{\partial z} \right) z = g \left(\frac{\partial \ln \rho_0}{\partial z} - \frac{1}{\gamma} \frac{\partial \ln p_0}{\partial z} \right) z \quad (7)$$

156 For the ideal gas law of $p = \rho RT$, the natural logarithm is taken for altitude, z on both sides,
 157 yielding

$$158 \quad \frac{\partial \ln \rho}{\partial z} = \frac{\partial \ln p}{\partial z} - \frac{\partial \ln T}{\partial z} \quad (8)$$

159 Then after, the potential temperature (θ) of the parcel is calculated as follows based on the
 160 equation (2):

$$161 \quad \frac{\partial \ln \theta}{\partial z} = \frac{\partial \ln T}{\partial z} - \frac{R}{c_p} \frac{\partial \ln p}{\partial z} = \frac{1}{T} \left(\frac{\partial T}{\partial z} + \frac{g}{c_p} \right) = \left(1 - \frac{R}{c_p} \right) \frac{\partial \ln p}{\partial z} - \frac{\partial \ln \rho}{\partial z} \quad (9) \text{ to derive the}$$

162 Parcels acceleration based on equations (7) to become:

$$163 \quad \frac{d^2s}{dt^2} = -g \frac{\partial \ln \theta_0}{\partial z} z \sin a = -g \frac{\partial \ln \theta_0}{\partial z} ds \cdot \sin^2 a \quad (10)$$

164 Whereas by introducing the frequency, N, with $N^2 = g \frac{\partial \ln \theta_0}{\partial z}$

165 The Brunt-Vaisala frequency, N^2 is calculated based on the following mathematical formulation
 166 used to characterize atmospheric stability/instability.

$$167 \quad N^2(z) = \frac{g(z)}{T_0(z)} \left(\frac{\partial T_0(z)}{\partial z} + \Gamma_d \right) \quad (11)$$

168 Where g is the acceleration due to gravity, N is the Vaisala frequency, T_0 is the background
 169 temperature (estimated based on third-order polynomial fitting), $\Gamma_d = g/c_p$ is the adiabatic lapse
 170 rate, and $c_p = 1004 J K^{-1} kg^{-1}$ is the specific heat capacity of the atmosphere at constant
 171 pressure. When the Väisälä frequency, N^2 , is positive, the atmosphere is stable whereas is
 172 negative, the atmosphere is unstable. When the Brunt-Väisälä frequency, N^2 , is positive the
 173 atmosphere is stable, whereas a negative N^2 indicates atmospheric instability. In this regard, the
 174 atmospheric lapse rate, $\Gamma = -\frac{\partial T}{\partial z}$, is larger than the adiabatic lapse rate, $g/c_p \approx 9.5 K km^{-1}$. A
 175 third-order least squares polynomial fit was applied to the SABER-observed temperature (T)
 176 profile to determine the background temperature (T_0), following the method outlined by Leblanc
 177 and Hauchecorne (1997). subsequently the perturbed temperature (T_p) is computed by
 178 subtracting the background temperature from the observed temperature data (T) in equation (12),

$$179 \quad T_p' = T - T_0 \quad (12)$$

180 After estimating the perturbed temperature (T_p), a high-pass band filter is applied. This filter
 181 removes low-frequency components associated with planetary and tidal waves, retaining the
 182 high-frequency components related to short-period gravity waves (John and Kumar, 2012). This
 183 process isolates the influence of gravity waves, enabling accurate calculation of their potential
 184 energy. The high-pass filter operates within known frequency ranges, typically below a one-hour
 185 period.

$$186 \quad E_p(z) = \frac{1}{2} \left(\frac{g(z)}{N(z)} \right)^2 \left(\frac{T_p'(z)}{T_0(z)} \right)^2 \quad (13)$$

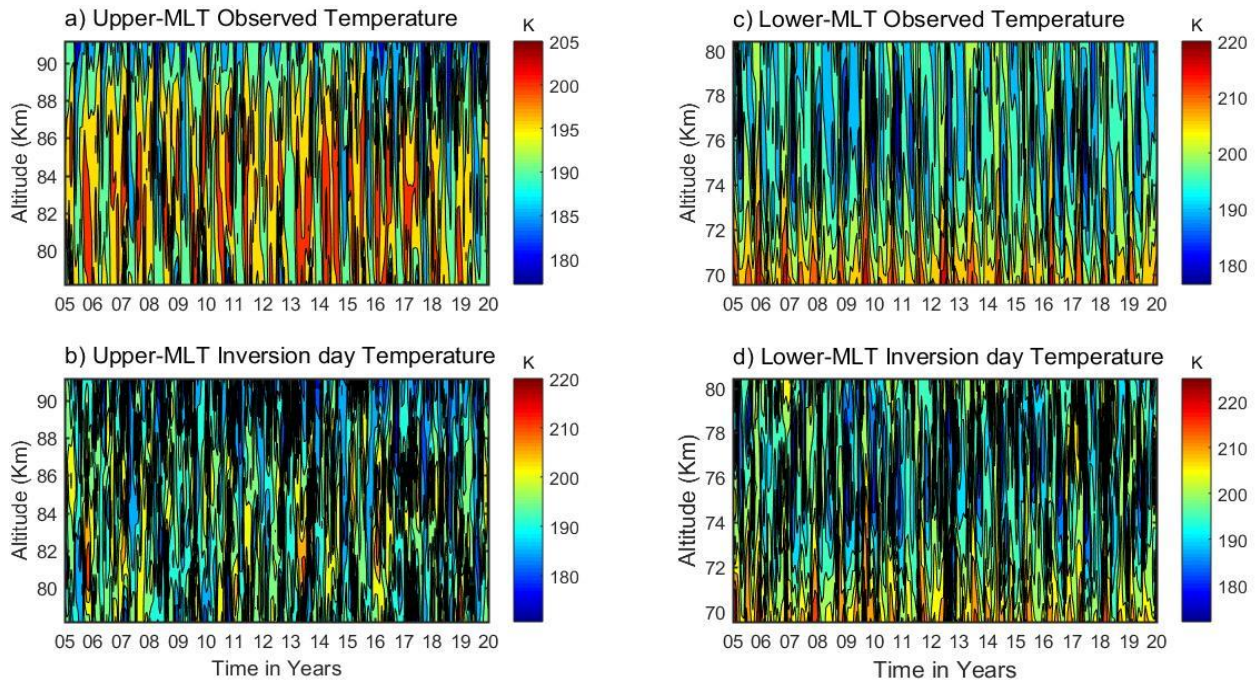
187 The potential energy of the waves, a function of altitude (z), is used to determine the
 188 impact of atmospheric gravity waves on atmospheric inversions.

189 3. Results and discussion

190 3.1 Identification and Characteristics of the Lower and Upper MLT Inversion

191 The SABER temperature profiles, covering altitudes of 60–100 km during 2005 to 2020, are
 192 shown in the contour plots of Figure 3. Figures 3(a and b) depict the upper MLT (mesospheric
 193 and lower thermospheric), while Figures 3(c and d) show the lower MLT region. The first

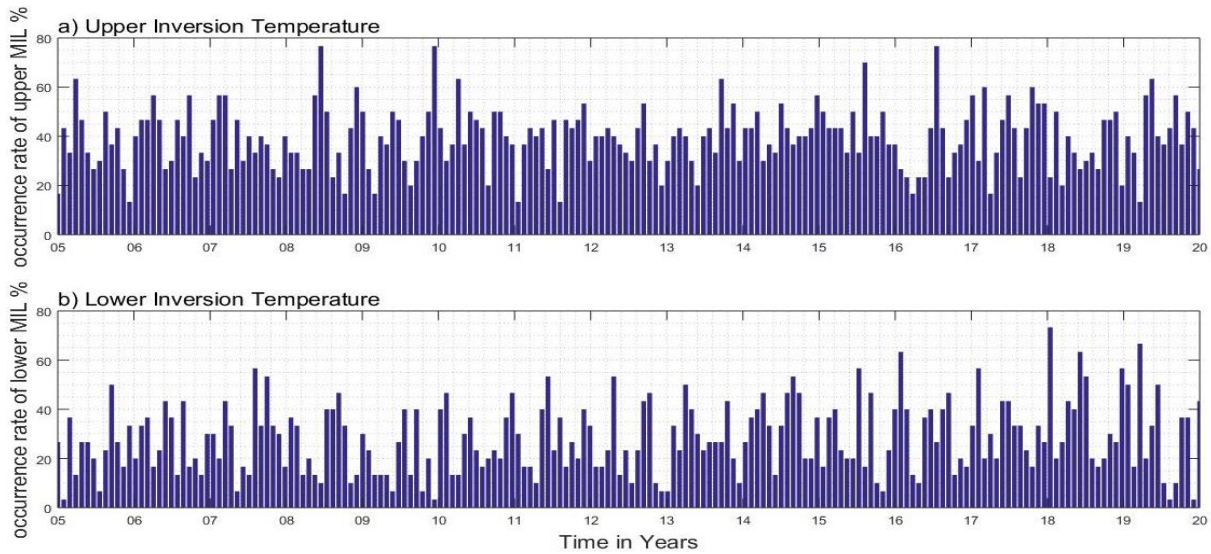
194 horizontal panel of Figures 3(a) and 3(c) show observed temperatures ranging from
 195 approximately 180–220 K, before accounting for inversion layers. Whereas, the second
 196 horizontal panel of Figures 3(b) and 3(d) show inversion day temperatures, ranging from 180–
 197 225 K.



198 **Figure 3.** The upper and lower mesosphere observed temperatures in the first horizontal panel at
 199 (a and c) with their inversions in the second horizontal panel at (b and d).
 200

201 The upper left panel of Figure 3(a) shows the observed temperature in the upper mesosphere
 202 ranges from approximately 180–205 K at altitudes of around 80–90 km. The upper right panel of
 203 Figure 3(c) shows the lower mesosphere, with temperatures ranging from about 180–220 K at
 204 altitudes of approximately 70–80 km. In contrast, the lower left panel of Figure 3(b) shows an
 205 upper-mesosphere inversion day temperature ranges from 180–220 K at an altitude of
 206 approximately 80–90 km. The lower right panel of Figure 3(d) shows a lower-mesosphere
 207 inversion day temperature, with the temperature ranging from 180–225 K at an altitude of
 208 approximately 70–80 km. These inversion day temperatures are higher than those shown in
 209 Figures 3(a) and 3(c). This indicates that maximum temperatures occur on inversion days in both
 210 the upper and lower MLT regions relative to the observed temperature. These inversion day
 211 temperatures in Figures 3(b) and 3(d) suggest a temperature gradient shifting from negative to
 212 positive. This could be due to factors such as atmospheric waves (planetary, tidal and particularly
 213 gravity waves), chemical reactions, or solar radiation. Our temperature observations for the
 214 lower MLT region on an inversion day, within the altitudinal range of 70–80 km, align with

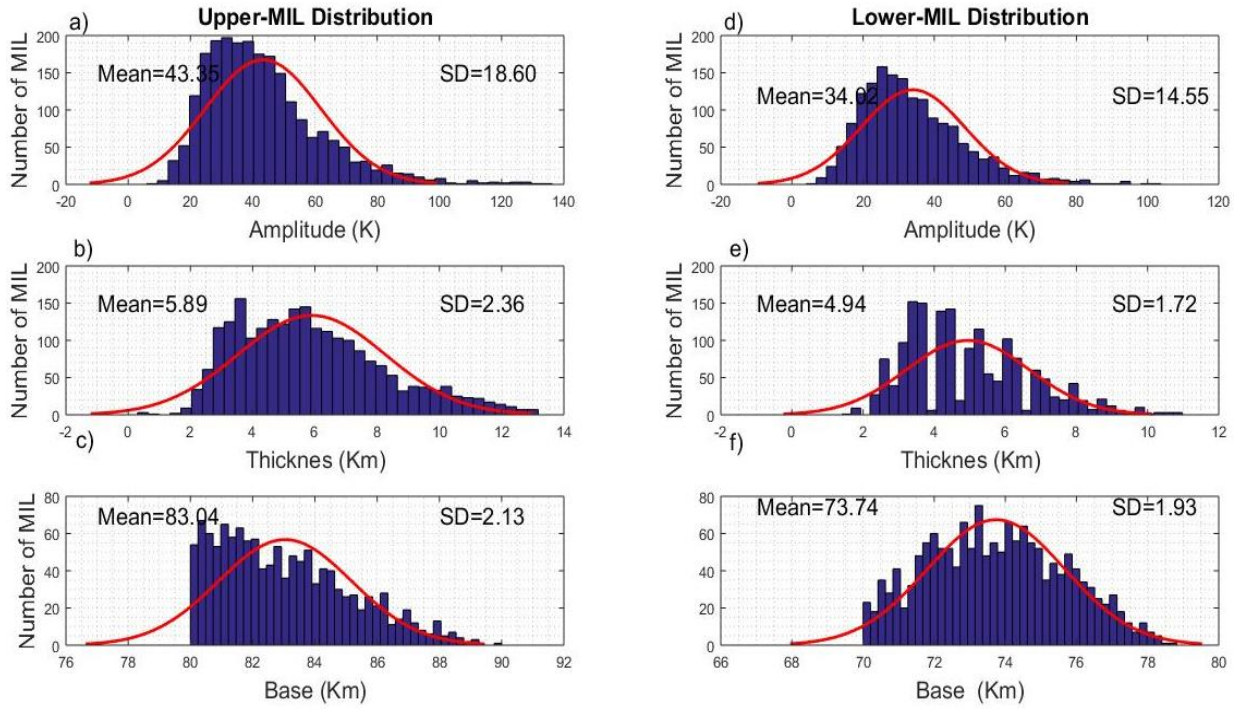
215 those reported by Sivakumar et al. (2001), who identified inversion day temperature variability
 216 in the altitudinal range of 73–79 km. Additionally, Sivakandan et al. (2014) examined
 217 mesospheric inversions in the 60–105 km altitude range over low-latitude regions; their findings
 218 closely match our results.



219 **Figure 4.** The frequency occurrence rate (percentage) of the (a) upper and (b) lower inversion
 220 temperatures during 2005-2020 over low latitudes.
 221

222 Figure 4 shows the frequency occurrence rate of mesospheric inversion layers (MILs) in
 223 histograms. Figure 4(a) shows the occurrence rate for upper MILs, while Figure 4(b) shows the
 224 rate for lower MILs. The mean frequency occurrence rate of upper inversions is approximately
 225 below 40%. Peak rates range from 60% to 78%, notably in the years 2008, 2010, and mid-2016.
 226 In contrast, the mean occurrence rate for lower inversions of Figure 4(b) is approximately below
 227 20%. The overall occurrence rate for upper inversions is relatively higher compared to lower
 228 inversions; this may be related to atmospheric wave activities, mainly gravity waves.
 229 Hauchecorne et al. (1987) and France et al. (2015) discuss the effects of gravity waves on
 230 inversion variability in the upper and lower mesosphere. Regarding these findings, Figure 5
 231 examines the characteristics of the inversion day temperature variability, based on their
 232 amplitude and thickness. It focuses on base height, amplitude, and thickness, before examining
 233 the effects of gravity waves on an inversion. Histograms display the frequency distribution of
 234 amplitude, thickness, and base height for MLT temperature variability on inversion days, with
 235 best-fit Gaussian distribution curves shown in red. The observed distributions align with
 236 Gaussian curves, indicating that the number of mesospheric inversion layers (MILs) follows a
 237 normal distribution. This suggests that the attributes are real-valued random variables. The left
 238 column has three rows showing histograms of (a) amplitude, (b) thickness, and (c) base height of

239 the inversion day temperature variability for the upper MLT. **These histograms also include the**
 240 **statistical metrics mean and standard deviations (SD) with their values.** The corresponding right
 241 column has three rows representing (d) amplitude, (e) thickness, and (f) base height of the
 242 inversion day temperature variability for the lower MLT region.



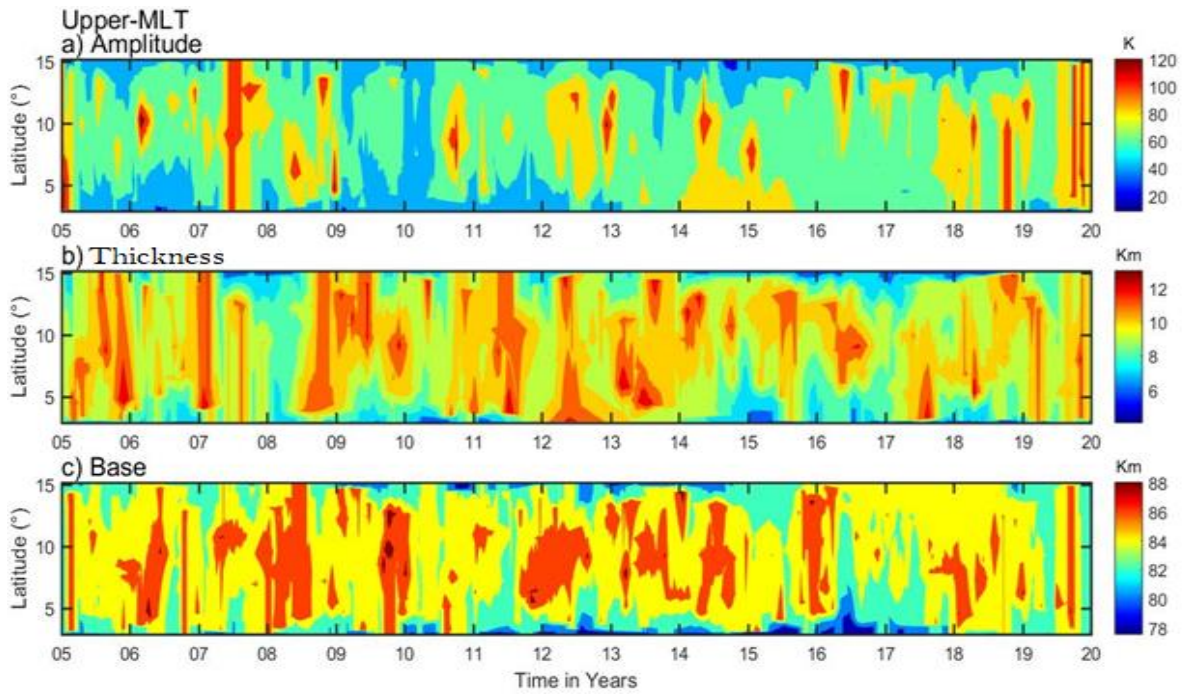
243 **Figure 5.** The histograms depict the occurrence of MLT inversion day temperature variability.
 244 The first vertical panel shows the distribution of (a) amplitude, (b) thickness, and (c) base height
 245 for the upper inversion day. The second vertical panel presents the corresponding distribution for
 246 the lower inversion, including (d) amplitude, (e) thickness, and (f) base height.
 247

248 The amplitude of upper inversion day temperature variability in Figure 5(a) ranges between 20
 249 and 80 K, with a peak value of 38 K. This follows a Gaussian distribution with a large standard
 250 deviation (SD) of 18.6, **which indicates high inversions.** The thickness of the inversion layer for
 251 upper MILs, shown in Figure 5(b), ranges from 3 to 9 K, and their most probable value is 5.5 K,
 252 with a low SD of 2.3. The base height of the upper MIL in Figure 5(c) spans from ~80 to 90 km,
 253 with a peak value of around 83 km. This indicates a large number of upper MLT inversions, with
 254 an SD of 2.13. The highest number of upper inversions between 2005 and 2020 is observed at 82
 255 km. This may be attributed to gravity wave breaking and energy dissipation, influenced by waves
 256 generated from lower atmospheric regions and solar flux impacts.

257 The lower inversion amplitude, shown in Figure 5(d), ranges from 10 to 60 K, with a peak value
258 of 25 K and a standard deviation (SD) of 14.5. The inversion thickness, as illustrated in Figure
259 5(e), spans 3 to 8 km, with the most likely value at 3.8 km and a low SD of 1.72. The base height
260 of the lower inversion in Figure 5(f) ranges from 70 to 80 km, with a peak value of around 74 km
261 and a lower SD of 1.93. Previous investigations by Sivakandan et al. (2014) from the Indian
262 sector reported amplitudes ranging from 14–39 K in 2002 and 15–42 K in 2008. The thicknesses
263 ranged between 2.7–7.5 km in 2002 and 2.8–7.3 km in 2008, under the influence of solar flux.
264 These findings align well with the present study, indicating no significant variation in
265 characterizing mesospheric inversion based on amplitude and thickness in the low-latitude region
266 within the altitude range of 60 to 90 km.

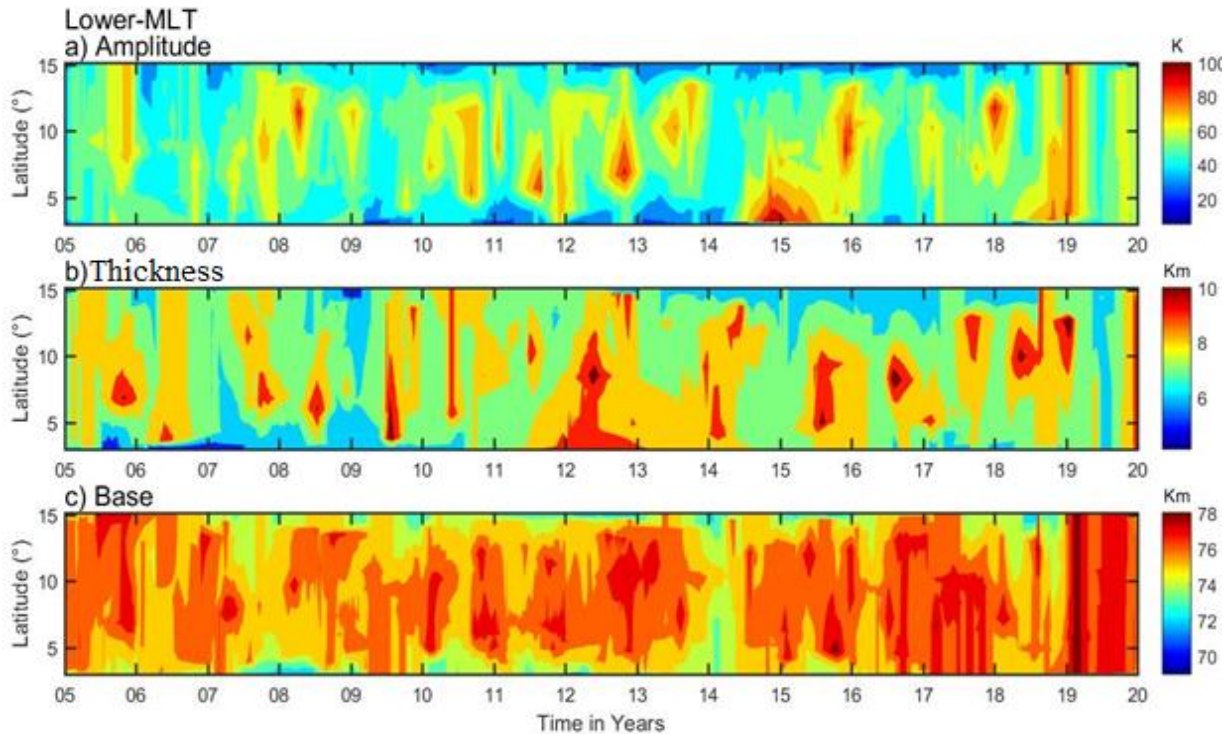
267 **3.2 Latitudinal Variations of Mesospheric Inversion Layers (MILs)**

268 This section examines the spatiotemporal variability of upper and lower mesosphere inversion
269 phenomena. Contour plots of time vs. latitude in Figures 6 and 7 show the variability of upper
270 and lower MLT inversion amplitude, thickness, and base height over the low-latitude band (3-
271 15°) during 2005–2020. The upper inversion is observed around 80–90 km; their maximum
272 amplitude, in the range of 90–120 K, occurs over latitude bands (5-12°) during 2005, 2007, mid-
273 2011, 2013, 2015, 2016, mid-2019, and 2020 (Figure 6(a)). The second horizontal panel of
274 Figure 6(b) shows the thickness, with a maximum range of ~(8–12 km) across the entire
275 latitudinal region (3-15° N). The third horizontal panel of Figure 6(c) shows the base height, with
276 relative maximum values around ~(84-88 km), in the latitudinal range between (4° & 14°) N
277 during 2006, 2008, 2010, 2012, 2016, and 2018.



278
 279 **Figure 6.** The daily upper inversions (~80-90 km) of (a) amplitude, (b) thickness, and (c) base
 280 height during 2005-2020 over latitudinal variation.

281 Whereas, the contour plots of Figure 7(a, b, and c) show the lower inversions (MILs) amplitude,
 282 thickness, and base height over an altitudinal range of ~70-80 km, respectively. Overall,
 283 amplitude values ranged from approximately 30-60 K across all latitudinal bands, reaching peak
 284 ranges of about 80-100 K during 2013, 2015, 2016, and 2019 in various latitude regions between
 285 5° and 14°N. The second horizontal panel of Figure 7(b) indicates thickness values ranging from
 286 5-7 km across the entire latitude band, with maximum thickness reaching 8-10 km in 2012-2013,
 287 2016, and 2019. The final horizontal panel of Figure 7(c) shows a base height of 76-80 km
 288 across most latitudes and periods, with notable exceptions in 2008, 2014, and mid-2018, where
 289 the base height reaches its maximum.



290

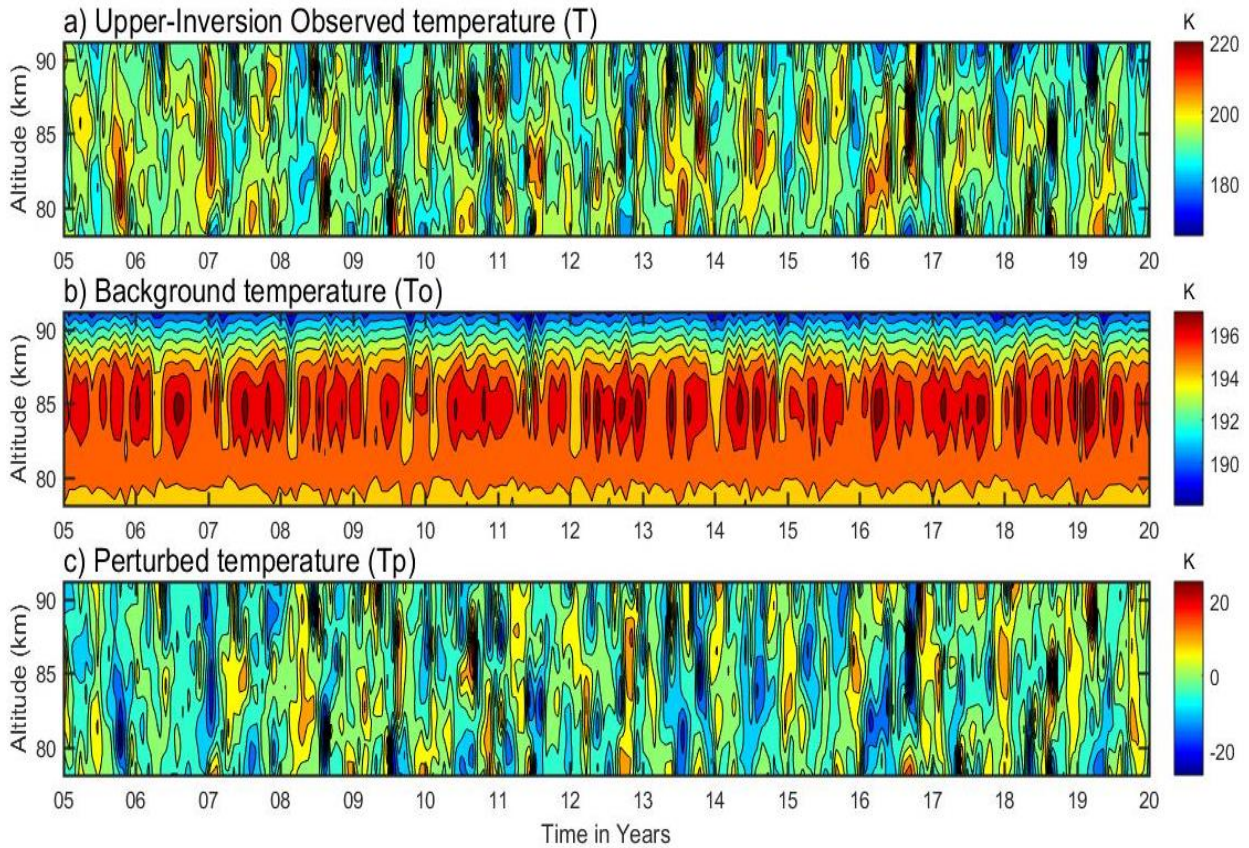
291 **Figure 7.** Same as Figure 5, but for the lower mesosphere inversions (~70- 80 km).

292 The higher amplitude and thickness are demonstrated in the upper and lower inversion to exhibit
 293 a suggested highly dynamic phenomenon. These valuable investigations are confirmed in Gan et
 294 al. (2012) based on SABER satellite observation at low latitudes.

295 **3.3 Analysis of Perturbed Temperature Variations in the MLT Region**

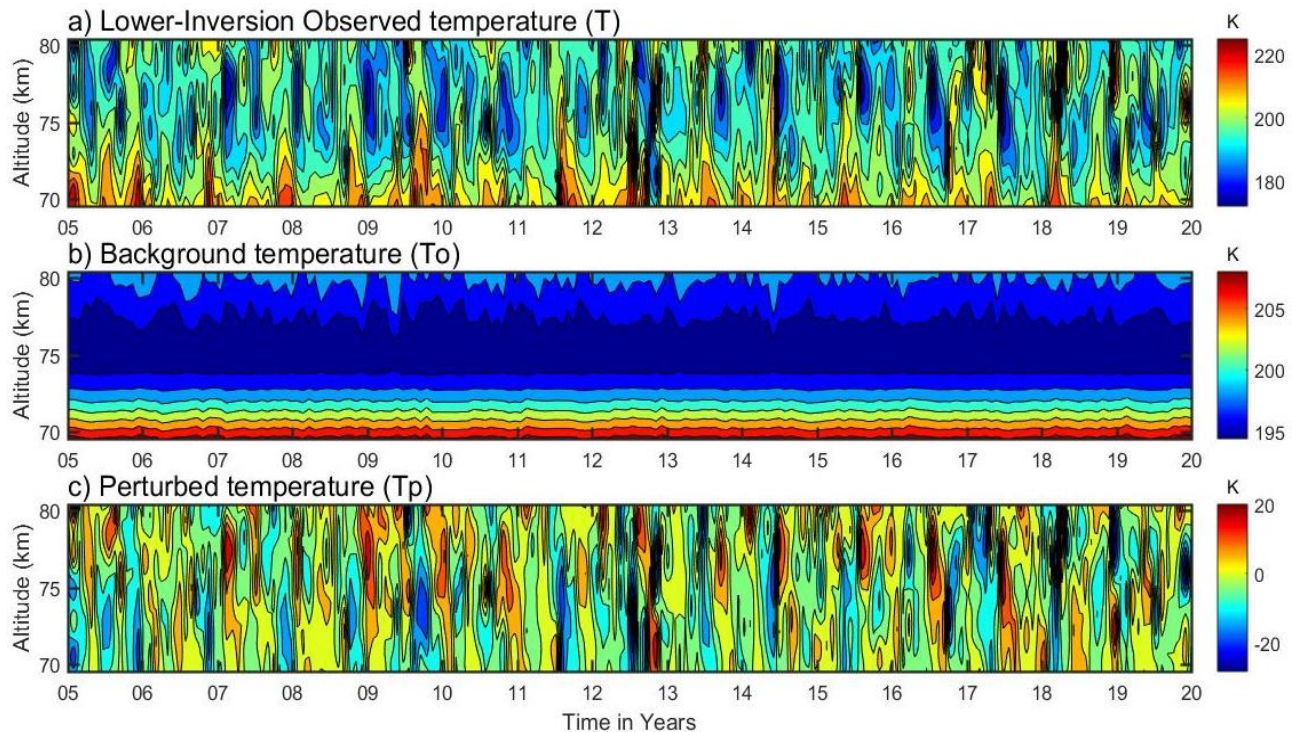
296 The perturbed temperature (T_p) of the upper and lower MLT inversions in Figure 8 and 9 can
 297 further be used to calculate their derived potential energy of gravity waves and the Brunt-Väisälä
 298 frequencies (N^2). First, the upper inversion profiles are identified in the MLT region during the
 299 entire observational period of 2005-2020, as displayed in the contour plot of Figure 8(a). Based
 300 on the observed temperature, which ranges from ~170 to 220 K with minimal variability, the
 301 background temperature is estimated. A 3rd-order polynomial fit is applied to calculate the
 302 background temperature (T_0), as shown in the contour plot of Figure 8(b). This maximum
 303 background temperature exhibits a periodic variability over an altitude of around ~82-87 km,
 304 ranging from ~195-197 K. The perturbed temperature profiles (T_p), determined by subtracting
 305 the background temperature profiles (T_0) from the observed inversion temperature (T), are in the
 306 range between -25 and +25 K, as illustrated in Figure 8(c).

307 The lower-MLT region perturbed temperature (T_p) is calculated using the same approach as the
308 upper-MLT perturbed temperature, using the observed and background temperatures. Their
309 corresponding contours are displayed in Figure 9(a-c).



310 **Figure 8.** The upper mesosphere temperatures in the vertical panel are: (a) inversion day
311 observed temperature; (b) background temperature; and (c) perturbed temperature in the upper
312 mesosphere region.
313

314 In Figure 9(a), the observed temperature of the lower inversion ranges from ~ 170 - 220 K.
315 Whereas, the background temperature of the lower inversion ranges from ~ 195 - 210 K, with
316 maximum values of ~ 200 - 210 K at a height of ~ 70 - 72 Km, as shown in Figure 9(b). The derived
317 lower-MLT perturbed temperature from the observed and background temperature is presented
318 in Figure 9(c) and ranges from -25 to 20 K. Notably, the upper-MLT perturbed temperature is at
319 its maximum compared to the lower-MLT region, possibly due to a highly dynamic
320 phenomenon.



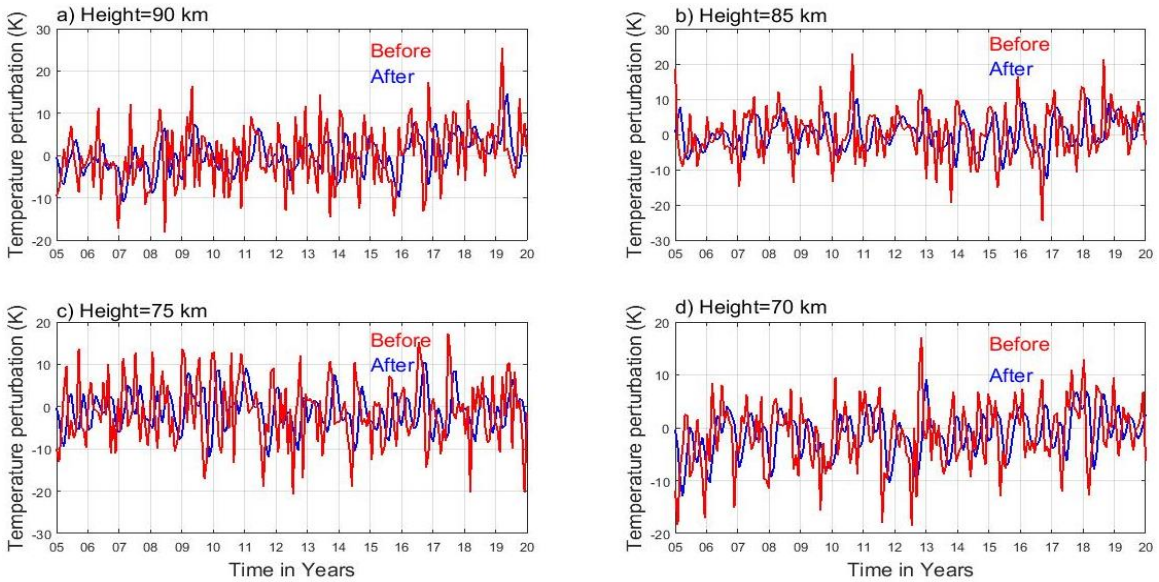
321
322 **Figure 9.** Same as Figure 7, but for the lower mesosphere atmospheric region.

323 **3.4 Effects of Gravity Waves on Mesosphere Inversions and Associated Instability**

324 **Atmospheric gravity waves** form when air parcels are oscillated due to the restoring force of
 325 gravity after being transported vertically. Several factors contribute to these waves, including
 326 airflow over mountains, convection, and wind shear. As the waves propagate vertically, they
 327 break and dissipate, releasing energy and momentum into the surrounding atmosphere, which
 328 contributes to the formation of inversion layers. **The gravity wave contribution is quantified by**
 329 **calculating the potential energy and assessing their impact on MLT instability through the Brunt-**
 330 **Väisälä frequency (N^2), derived from perturbed temperature (T_p') data spanning 2005–2020.**
 331 **Several authors (Tsuda et al., 2000; Wang and Geller, 2003; Liu et al., 2014; Thurairajah et al.,**
 332 **2014) suggest that gravity wave activity is represented by potential energy. Further investigation**
 333 **is required, focusing on altitudes of 90, 85, 75, and 70 km, to evaluate the impacts of gravity**
 334 **waves on an inversion by applying a high-pass filter with a one-hour interval to the T_p' data (see**
 335 **Figure 10 a-d). The high-pass filter attenuates low-frequency components, removing the effects**
 336 **of long-period wave oscillations, such as tidal and planetary wave contributions. This effectively**
 337 **isolates the gravity waves (Gw), allowing a clearer focus on their impact on MLT inversions, as**
 338 **appeared in Figure 10.**

339 **The blue curve in Figure 10(a to d) appears smoother after applying the high-pass filter to the**
 340 **perturbed temperature. However, the filter removes the peaks of low-frequency variations,**

341 resulting in retained perturbed temperature values that appear more uniform, creating a smooth
 342 plateau effect. In the upper mesosphere (90 and 85 km), the filter reduces the amplitude of wave
 343 oscillations from approximately ± 20 K to ± 10 K, as shown from the blue curve in Figure 10a and
 344 b, compared to the red curve. Similarly, in the lower mesosphere (75 and 70 km) at (Figure 10 c
 345 & d) the amplitude decreases from $\sim(-20$ to 20 K) to $\sim(-8$ to 8 K) by filtering out higher
 346 amplitudes.

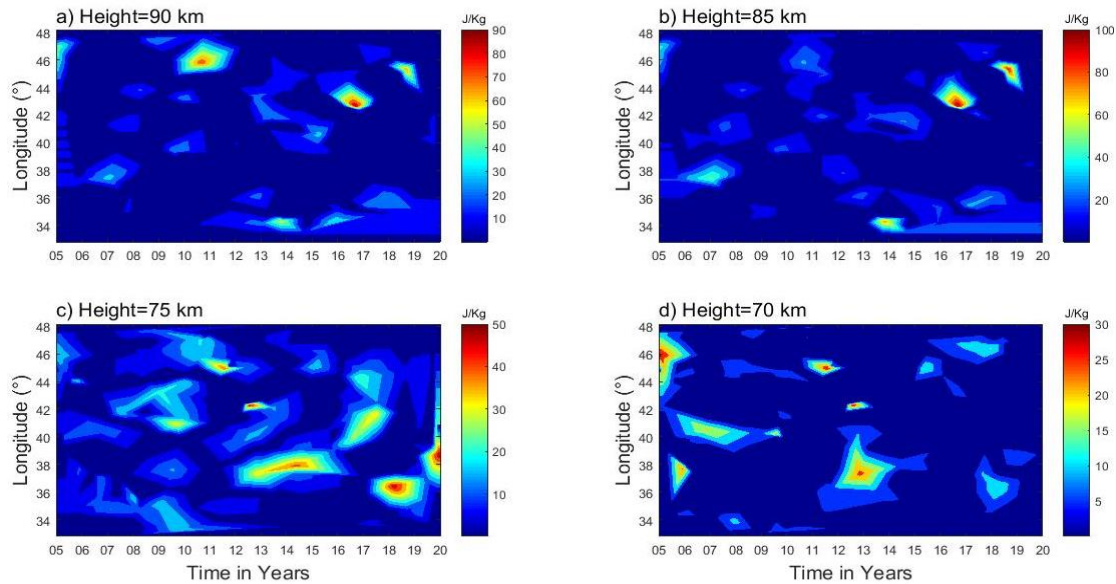


347 **Figure 10.** Perturbed temperature profiles before (red color) and after (blue color) applying the
 348 high-pass filter for the upper (90 and 85 km) and lower (75 and 70 km) regions.
 349

350 In the MLT atmospheric region, gravity wave breaking typically dissipates their potential and
 351 kinetic energy, leading to increased turbulence and mixing. As illustrated, gravity wave
 352 propagation and dissipation are major forces in the MLT (Lindzen, 1981; Holton, 1983),
 353 influencing the middle and upper atmospheric regions. This has a substantial impact on the
 354 overall dynamics as well as the MLT's thermal structure, particularly the increase in temperature
 355 variability with elevation, known as inversion. Holton et al. (2003) and Holton and Hakim
 356 (2013) has demonstrated an interaction between the potential energy of gravity waves and
 357 inversions. This notable upper and lower inversions are observed in Figure 4 during the period
 358 2005–2020 over the low-latitude regions. During this period, particularly for the upper-MLT
 359 region above 80 km altitude, high-resolution SABER satellite temperature data revealed the
 360 presence of a strong mesospheric inversion layer (MIL), with peak occurrence rates ranging
 361 between 60% and 78%, especially during 2010, 2014, 2016/17, and 2018/19, Figure 4a.
 362 Correspondingly, at the same time and in the same region (upper-MLT), at altitudes of 85 and 90
 363 km, there is a noticeable increase in gravity wave potential energy (E_p), shown in Figure 11. The

364 maximum potential energy (PE) for the upper-MLT region corresponds to the breaking or
365 dissipation of gravity waves as they propagate upward. This spike in potential energy coincides
366 with the occurrence of the inversion layer, suggesting that the breaking or dissipation of gravity
367 waves releases energy into the atmosphere, contributing to localize heating in the mesosphere
368 and leading to the formation of the inversion. The sudden transfer of momentum and energy
369 from the breaking GWs to the surrounding atmosphere disrupts the thermal structure, causing the
370 temperature inversion. In this case, the temporal and spatial coincidence between the peak in
371 gravity wave potential energy and the formation of the inversion demonstrates a clear physical
372 connection. The energy released from breaking GWs plays a direct role in the creation of the
373 inversion layer, as shown in Figures 4 and 11. Similarly, the statistical distributions of upper-
374 MLT inversions in Figure 5(a) show maximum amplitudes, which correspond to the maximum
375 potential energy of gravity waves in Figure 11(a & b). This provides a straightforward
376 demonstration of how gravity wave dynamics-specifically, the dissipation of their potential
377 energy-are linked to the formation of mesospheric inversion layers (MILs).

378 Figure 11 (a-d) demonstrates that the spatiotemporal variability of gravity wave potential energy,
379 showing over the upper-MLT at (90 and 85 km) and the lower-MLT at (75 and 70 km). Figure
380 11(a) of upper-MLT inversions at 90 km shows maximum gravity wave potential energies,
381 ranging from ~70 to 90 J/kg, over the longitudinal regions of 45-47° E, as well as at 43° E, and
382 44° E during 2011, 2017, and 2019. In contrast, potential energies being the least in amount
383 around ~10 to 60 J/kg are present across the entire longitudinal region from 33-48° E. Figure
384 11(b) of upper-MLT region shows maximum potential energies of ~70 to 100 J/kg over the
385 longitudinal regions of 34°, 44°, and 46° E during 2014, 2016, and 2018 at 85 km. Its minimum
386 potential energies between 20 and 70 J/kg appear over the longitude regions from 33-48° E.
387 Whereas, Figures 11(c) and 11(d) depict the gravity wave potential energy in the lower-MLT
388 regions at 75 and 70 km, respectively. At 75 km, Figure 11(c) shows a relative maximum
389 potential energy of 40-50 J/kg over the longitudinal regions of 46°, 42°, 40°, 37°, 36°, and 38° E
390 during 2011, 2012, 2017, 2013–2015, 2018, and 2020. Similarly, Figure 11(d) illustrates gravity
391 wave potential energy ranging from 2-30 J/kg at 70 km across the longitudinal region of 33-48°
392 E. Their maximum potential energy of 25-30 J/kg is observed in certain longitudinal regions over
393 time.

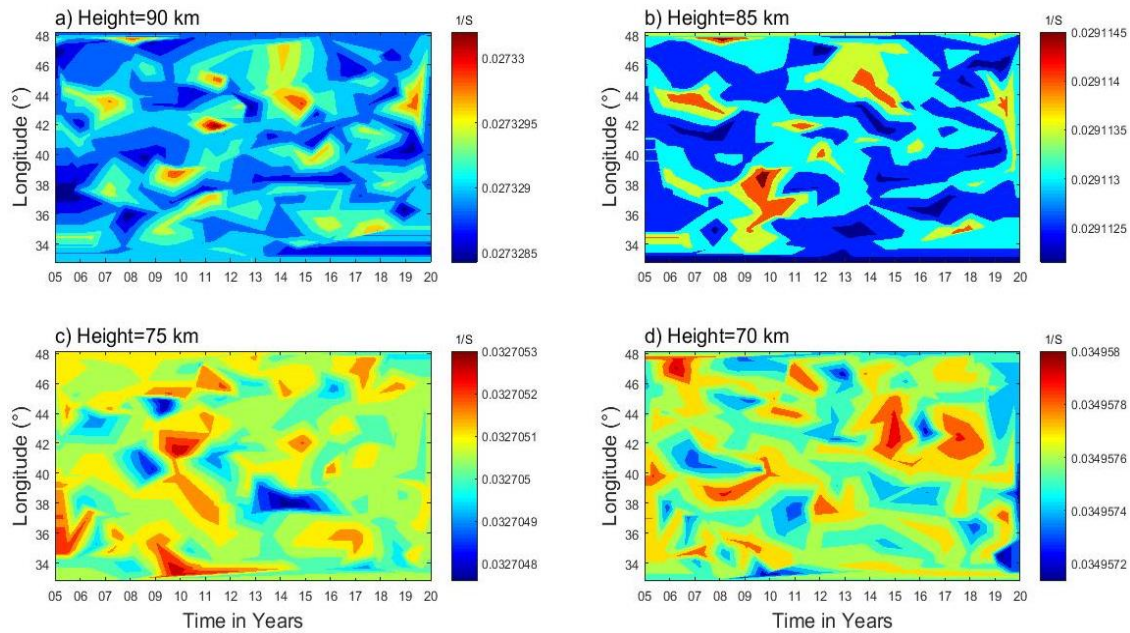


394

395 **Figure 11.** Gravity wave potential energy for the upper (90 and 85 km) and lower (75 and 70
 396 km) MLT regions.

397 The role of gravity waves in the MLT region instability, the Brunt-Väisälä frequency is
 398 analysed. Contour plots in Figure 12 (a-d) show the spatiotemporal variability of the Brunt-
 399 Väisälä frequency, with Figures 12(a and b) representing the **upper-MLT** (90 and 85 km) and
 400 Figures 12(c and d) representing the **lower-MLT** (75 and 70 km). The Brunt-Väisälä frequency
 401 (N^2) shows that the upper MLT region is more unstable (~ 0.027 at 90 km and ~ 0.029 at 85 km)
 402 **relative to that of the lower MLT region** (~ 0.033 at 75 km and ~ 0.035 at 70 km). **These different**
 403 **values of brunt-vaiala frequency under a quencyquence of gravity waves generation in different**
 404 **sizes**, with smaller waves being the main drivers of instability and turbulence in the MLT
 405 (mesosphere and lower thermosphere) region (Liu and Meriwether, 2004; Szewczyk et al.,
 406 2013). Hauchecorne et al. (1987) proposed a model where a series of breaking gravity waves
 407 leads to the formation of MILs through the gradual accumulation of heat, which contributes to
 408 instability. Conducting mesospheric inversion layer (MIL) phenomena is crucial for
 409 understanding MLT atmospheric dynamics, especially when it comes to stability and energy
 410 transfer.

411



412

413 Figure 12. Brunt-Väisälä frequency (N^2) variability for the upper (90 and 85 km) and lower (75
 414 and 70 km) MLT regions.

415 **4 Summary**

416 In this article, 16 years of SABER MLT temperature profiles are utilized to investigate the MIL
 417 phenomenon and its causative mechanism through gravity wave potential energy (P_E) and
 418 instability criteria of Brunt-Väisälä frequency (N^2) over low-latitudes. The following conclusions
 419 are drawn from the observations in this article:

- 420 ✓ The upper mesosphere inversion frequency occurs more often than the lower mesosphere
 421 inversion.
- 422 ✓ Analysis of the MIL characteristic features reveals the most probable values for the upper
 423 inversion: amplitude of 38 k, thickness of 5.5 km, and base height of 78 km. The lower
 424 inversion has an amplitude of 25 K, a thickness of 3.8 km, and a base height of 73 km.
- 425 ✓ The upper mesosphere region has higher gravity wave potential energy compared to the
 426 lower mesosphere region.
- 427 ✓ The high potential energy in the upper mesosphere region is likely due to the deposition of
 428 energy and momentum by gravity wave breaking. This could influence the dynamics of the
 429 inversion phenomenon.
- 430 ✓ The Brunt-Väisälä frequency (N^2) indicates that the upper mesosphere region is less stable
 431 than the lower mesosphere region. This lower stability contributes to the high potential
 432 energy in the upper mesosphere, which leads to larger inversion phenomena.

433 ✓ Atmospheric processes vary significantly from region to region, with altitude, and over time.

434 **Data availability.** The SABER data are freely available via the link at [http://saber.gats-inc.com/](http://saber.gats-inc.com/index.php)
435 [index.php](http://saber.gats-inc.com/index.php).

436 **Author contribution.** Chalachew Lingerew: data curation, investigation, software,
437 visualization, writing the original draft, and writing review. U. Jaya Prakash Raju; supervision,
438 and editing.

439 **Competing interest.** The authors declare that they have no conflict of interest relevant to this
440 study.

441 **Acknowledgments.** The Authors would like to express their gratitude to the National Aeronautics
442 and Space Administration (NASA) for providing the SABER data from the website:
443 <http://saber.gats-inc.com/index.php>.

444 **References**

445 Begue, N., Mbatha, N., Bencherif, H., Loua, R. T., Siva Kumar, V., & Leblanc, T.: Statistical
446 analysis of the mesospheric inversion layers over two symmetrical tropical sites:
447 Reunion (20.8° S, 55.5° E) and Mauna Loa (19.5° N, 155.6° W). *In Annales Geophysicae*,
448 35, 1177-1194, 2017.

449 Bizuneh, C.L., Prakash, R., and Nigussie, M.: Long-term temperature and ozone response to
450 natural drivers in the mesospheric region using 16 years (2005–2020) of TIMED/SABER
451 observation data at 5-15°N. *Advances in Space Research*, 70, 2095–2111,
452 <https://doi.org/10.1016/j.asr.2022.06.051>, 2022.

453 Collins, R. L., Lehmacher, G. A., Larsen, M. F., and Mizutani, K.: Estimates of vertical eddy
454 diffusivity in the upper mesosphere in the presence of a mesospheric inversion layer, *Ann.*
455 *Geophys.*, 29(11), 2019–2029, <http://doi:10.5194/angeo-29-2019-2011>, 2011.

456 Cutler, L. J., Collins, R. L., Mizutani, K., and Itabe, T.: Rayleigh lidar observations of
457 mesospheric inversion layers at Poker Flat, Alaska (65° N, 14° W), *Geophys. Res. Lett.*, 28,
458 1467–1470, <https://doi.org/10.1029/2000GL012535>, 2001.

459 Dou, X., Li, T., Xu, J., Liu, H. L., Xue, X., Wang, S., Leblanc, T., McDermid, I. S.,
460 Hauchecorne, A., Keckhut, P., Bencherif, H., Heinselman, C., Steinbrecht, W., Mlynczak, M.
461 G., and Russell III, J. M.: Seasonal oscillations of middle atmosphere temperature observed by
462 Rayleigh lidars and their comparisons with TIMED/SABER observations, *J. Geophys. Res.*,
463 114, D20103, <https://doi.org/10.1029/2008JD011654>, 2009.

464 Duck, T. J., Sipler, D. P., and Salah, J. E.: Rayleigh lidar observations of a mesospheric
465 inversion layer during night and day, *Geophys. Res. Lett.*, 28, 3597–3600, 2001.

466 Duck, T. J. and Greene, M. D.: High Arctic observations of mesospheric inversion layers,
467 *Geophys. Res. Lett.*, 31, L02105, <https://doi.org/10.1029/2003GL018481>, 2004.

468 Eckermann, S.D., Hirota, I., and Hocking, W. K.: Gravity wave and equatorial wave morphology
469 of the stratosphere derived from long-term rocket soundings. *Q. J. R. Meteorol. Soc.*, 121, 149
470 186, <http://doi.org/10.1002/qj.49712152108>, 1994.

471 Emanuel, K.A.: *Atmospheric Convection*, Oxford University Press, New York, 580pp, 1994.

472 Fechine, J., Wrasse, C. M., Takahashi, H., Mlynczak, M. G., and Russell, J. M.: Lower-
473 mesospheric inversion layers over Brazilian equatorial region using TIMED/SABER
474 temperature profiles, *Adv. Space Res.*, 41, 1447–1453, [https://doi.org/10.1016/j.asr.2007.](https://doi.org/10.1016/j.asr.2007.04.070)
475 04.070, 2008.

476 Fritts, D. C., Wang, L., Laughman, B., Lund, T. S., & Collins, R. L.: Gravity wave dynamics in a
477 mesospheric inversion layer: 2. Instabilities, turbulence, fluxes, and mixing. *Journal of*
478 *Geophysical Research: Atmospheres*, 123, 649–670, <https://doi.org/10.1002/2017JD027442>,
479 2018.

480 France, J. A., Harvey, V. L., Randall, C. E., Collins, R. L., Smith, A. K., Peck, E. D., and Fang,
481 X.: A climatology of planetary wave-driven mesospheric inversion layers in the extratropical
482 winter, *J. Geophys. Res.-Atmos.*, 120, 399–413, <https://doi.org/10.1002/2014JD022244>, 2015.

483 Fritts, D. C., and Alexander, M. J.: Gravity wave dynamics and effects in the middle atmosphere,
484 *Rev. Geophys.*, 41, 1003, <https://doi.org/10.1029/2001RG000106>, 2003.

485 Fritts, D. C., Laughman, B., Wang, L., Lund, T. S., & Collins, R. L.: Gravity wave dynamics in a
486 mesospheric inversion layer: 1. Reflection, trapping, and instability dynamics. *Journal of*
487 *Geophysical Research: Atmospheres*, 123, 626–648, <https://doi.org/10.1002/2017JD027440>,
488 2018.

489 Gan, Q., Zhang, S. D., and Yi, F.: TIMED/SABER observations of lower mesospheric inversion
490 layers at low and middle latitudes, *J. Geophys. Res.*, 117, D07109, [https://doi.org/10.1029/2012JD](https://doi.org/10.1029/2012JD017455)
491 017455, 2012.

492 Garcia-Comas, M., Lopez-Puertas, M., Marshall, B. T., Winter Steiner, P. P., Funke, B.,
493 Bermejo-Pantaleon, D., Mertens, C. J., Remsberg, E. E., Gordley, L. L., Mlynczak, M. G., and
494 Russell III, J. M.: Errors in Sounding of the Atmosphere using Broadband Emission
495 Radiometry (SABER) kinetic temperature caused by non-local-thermodynamic-equilibrium
496 model parameters, *J. Geophys. Res.*, 113, D24106, doi: 10.1029/2008JD010105, 2008.

497 Hirota, I.: Climatology of gravity waves in the middle atmosphere. *J. Atmos. Terr. Phys.*, 46,
498 767–773, <http://doi.org/10.2151/jmsj1965.63.6-1055>, 1984.

499 Hamilton, K.: Climatological Statistics of Stratospheric Inertia-Gravity Waves Deduced from
500 Historical Rocket-sonde Wind and Temperature Data. *J. Geophys. Res.*, 96, 20831–20839,
501 <http://doi.org/10.1029/91JD02188>, 1991.

502 Hauchecorne, A., Chanin, M. L., & Wilson, R.: Mesospheric temperature inversion and
503 gravity wave breaking. *Geophysical Research Letters*, 14(9), 933-936, [https://doi.org/10.1029/
504 GL014i009p00933](https://doi.org/10.1029/GL014i009p00933), 1987.

505 Holton, J. R., Curry, J. A., and Pyle, J. A.: *Encyclopedia of atmospheric sciences*, volume 1.
506 Academic Press, 2003.

507 Holton, J. R.: The influence of gravity wave breaking on the general circulation of the middle
508 atmosphere, *J. Atmos. Sci.*, 40, 2497–2507, 1983.

509 Holton, J. R. and Hakim, G. J.: *An introduction to dynamic meteorology*. Academic Press, 2013.

510 Irving, B. K., Collins, R. L., Lieberman, R. S., Thurairajah, B., and Mizutani, K.: Mesospheric
511 Inversion Layers at Chatanika, Alaska (65°N, 147°W): Rayleigh lidar observations and
512 analysis, *J. Geophys. Res. Atmos.*, 119, 11,235–249, <http://doi:10.1002/2014JD021838>, 2014.

513 John, S.R., Kumar, K. K.: TIMED/SABER observations of global gravity wave climatology and
514 their interannual variability from stratosphere to mesosphere lower thermosphere. *Clim. Dyn.*,
515 39, 1489–1505, <http://doi.org/10.1007/s00382-012-1329-9>, 2012.

516 Leblanc, T., McDermid, I. S., Hauchecorne, A., and Keck hut, P.: Evaluation of optimization of
517 lidar temperature analysis algorithms using simulated data, *J. Geophys. Res.*, 103, 6177–6187,
518 1998.

519 Leblanc, T., and Hauchecorne, A.: Recent observations of mesospheric temperature inversions, *J.*
520 *Geophys. Res.*, 102, 19471–19482, <https://doi.org/10.1029/97JD01445>, 1997.

521 Lindzen, R. S.: Turbulence and stress due to gravity waves and tidal breakdown, *J. Geophys.*
522 *Res.*, 86, 9707–9714, <https://doi:10.1029/JC086iC10p09707>, 1981.

523 Lingerew, C., Jaya Prakash Raju, U., & Guimarães Santos, C. A.: NN-MLT model prediction for
524 low-latitude region based on artificial neural network and long-term SABER observations.
525 *Earth and Space Science*, 10, e2023EA002930, <https://doi.org/10.1029/2023 EA002930>, 2023.

526 Liu, S-D., and S-S. Liu: *Atmosphere Dynamics*, Peking University Press, Beijing, 2011.

527 Liu, H. L., Hagan, M. E., & Roble, R. G.: Local mean state changes due to gravity wave
528 breaking modulated by the diurnal tide. *Journal of Geophysical Research*, 105(D10),
529 12381-12396, (2000).

530 Liu, H. L., & Hagan, M. E.: Local heating/cooling of Atmospheres. 96(D8), 15297-15309,
531 (1998).

532 Mlynczak, M. G., Marshall, B. T., Martin-Torres, F. J., Russell III, J. M., Thompson, R. E.,
533 Remsberg, E. E., and Gordley, L. L.: Sounding of the Atmosphere using Broadband Emission
534 Radiometry observations of daytime mesospheric O₂ (1Δ) 1.27 μm emission and derivation of
535 ozone, atomic oxygen, and solar and chemical energy deposition rates, 2007.

536 Meriwether, J. W., and Gerrard, A. J.: Mesosphere inversion layers and stratosphere temperature
537 enhancements, *Rev. Geophys.*, 42, RG3003, <http://doi:10.1029/2003RG000133>, 2004.

538 Meriwether, J. W., and Gardner, C. S.: A review of the mesosphere inversion layer phenomenon,
539 *J. Geophys. Res.*, 105, 12 405–12 416, 2000.

540 Nath, O., & Sridharan, S.: Long-term variabilities and tendencies in zonal mean TIMED–
541 SABER ozone and temperature in the middle atmosphere at 10–15°N. *Journal of Atmospheric
542 and Solar-Terrestrial Physics*, 120, 1–8, <https://doi:10.1016/j.jastp.2014.08.010>, 2014.

543 Ramesh, K., Sridharan, S.: Large mesospheric inversion layer due to breaking of small scale
544 gravity waves: Evidence from Rayleigh lidar observations over Gadanki (13.51⁰ N, 79.21⁰ E).
545 *J. Atmos. Sol. Terr. Phys.* 89, 90–97, <http://doi.org/10.1016/j.jastp.2012.08.011>, 2012.

546 Ramesh, K., Sridharan, S. and Vijaya Bhaskara, S.: Causative mechanisms for the occurrence of
547 a triple-layered mesospheric inversion event over low latitudes, *J. Geophys. Res. Space
548 Physics*, 119, 3930–3943, <http://doi:10.1002/2013JA019750>, 2014.

549 Ramesh, K., Sridharan, S., Raghunath, K., and Rao, S. V. B.: A chemical perspective of day and
550 night tropical (10°N–15°N) mesospheric inversion layers, *J. Geophys. Res. Space Physics*,
551 122, <http://doi:10.1002/2016JA023721>, 2017.

552 Ramesh, K., Sridharan, S., Vijaya Bhaskara Rao, S., Raghunath, K., Bhavani Kumar, K.:
553 Rayleigh lidar observations of mesospheric inversion layers over Gadanki (13.5⁰N, 79.2⁰ E)
554 and their relation with gravity wave activities. *Indian Journal of Radio and Space Science*, 43,
555 83-90, 2013.

556 Remsberg, E., Lingenfelter, V., Harvey, V., Grose, W., Russell III, J., Mlynczak, M., Gordley,
557 L., and Marshall, B. T.: The verification of the quality of SABER temperature, geopotential
558 height, and wind fields by comparison with Met Office assimilated analyses, *J. Geophys. Res.*,
559 108(D19), 4628, <https://doi:10.1029/2003JD003720>, 2003.

560 Rezac, L., Kutepov, A., Russell, J.M., Feofilov, A.G., Yue, J., and Goldberg, R.A.: Simultaneous
561 retrieval of T (p) and CO₂ VMR from two-channel non-LTE limb radiances and application to

562 daytime SABER/ TIMED measurements. *J. Atmos. Sol. Terr. Phys* 130–131, 23–42.
563 <https://doi.org/10.1016/j.jastp.2015.05.004>, 2015.

564 Russell, J.M., Mlynczak, M.G., Gordley, L.L., Tansock, J., Esplin, R.: An overview of the
565 SABER experiment and preliminary calibration results. In *Proceedings of the SPIE*, 44th
566 Annual Meeting, Denver, CO, USA, 3756, 277–288, 1999.

567 Schmidlin, F. J.: Temperature inversions near 75 km. *Geophysical Research Letters*, 3(3),
568 173-176, (1976).

569 Sica, R. J., Argall, P. S., Shepherd, T. G., and Koshyk, J. N.: Model-measurement comparison of
570 mesospheric temperature inversions, and a simple theory for their occurrence, *Geophys. Res.*
571 *Lett.*, 34, L23806, <https://doi.org/10.1029/2007GL030627>, 2007.

572 Sivakandan, M., Kapasi, D., and Taori, A.: The occurrence altitudes of middle atmospheric
573 temperature inversions and mesopause over low-latitude Indian sector, *Ann. Geophys.*, 32,
574 967–974, <https://doi.org/10.5194/angeo-32-967-2014>, 2014.

575 Siva Kumar, V., Bhavani Kumar, Y., Raghunath, K., Rao, P. B., Krishnaiah, M., Mizutani, K.,
576 Aoki, T., Yasui, M., and Itabe, T.: Lidar measurements of mesospheric temperature inversion
577 at a low latitude, *Ann. Geophys.*, 19, 1039–1044, <https://doi.org/10.5194/angeo-19-1039-2001>,
578 2001.

579 Sridharan, S., Sathishkumar, S., and Gurubaran, S.: Influence of gravity waves and tides on
580 mesospheric temperature inversion layers: simultaneous Rayleigh lidar and MF radar
581 observations, *Ann. Geophys.*, 26, 3731–3739, 2008.

582 Singh, R. P., & Pallamraju, D.: Mesospheric temperature inversions observed in OH and O2
583 rotational temperatures from Mount Abu (24.6°N, 72.8°E), India. *Journal of Geophysical*
584 *Research: Space Physics*, 123, 8823–8834, <https://doi.org/10.1029/2018JA025703>, 2018.

585 Smith, A.: Global Dynamics of the MLT, *Surv. Geophys*, 33, 1177–1230,
586 <https://doi.org/10.1007/s10712-012-9196-9>, 2012.

587 Szewczyk, A., Strelnikov, B., Rapp, M., Strelnikova, I., Baumgarten, G., Kaifler, N., Dunker, T.,
588 and Hoppe, U. P.: Simultaneous observations of a Mesospheric Inversion Layer and turbulence
589 during the ECOMA-2010 rocket campaign, *Ann. Geophys.*, 31, 775–785, [http://doi.org/10.5194/](http://doi.org/10.5194/angeo-31-775-2013)
590 [angeo-31-775-2013](http://doi.org/10.5194/angeo-31-775-2013), 2013.

591 Vadas, S. L., and Fritts, D. C.: Thermosphere responses to gravity waves: Influences of
592 increasing viscosity and thermal diffusivity, *J. Geophys. Res.*, VOL. 110, D15103, doi:
593 [10.1029/2004JD005574](https://doi.org/10.1029/2004JD005574), 2005.

594 Wang, L., Geller, M.A., Alexander, M.J.: Spatial and Temporal Variations of Gravity Wave
595 Parameters. Part I: Intrinsic Frequency, Wavelength, and Vertical Propagation Direction. *J.*
596 *Atmos. Sci.*, 62, 125–142, <http://doi.org/10.1029/2010JD013860>, 2005.

597 Wang, L., and Alexander, M.J.: Global estimates of gravity wave parameters from GPS radio
598 occultation temperature data. *J. Geophys.Res.* 115, D21122, <http://doi.org/10.1029/2010J>
599 [D013860](http://doi.org/10.1029/2010JD013860), 2010.

600 Walterscheid, R. L., and Hickey, M. P.: Gravity wave ducting in the upper mesosphere and lower
601 thermosphere duct system, *J. Geophys. Res.*, 114, D19109, <http://doi:10.1029/2008JD011269>,
602 2009.

603 Yuan, T., Pautet, P. D., Zhao, Y., Cai, X., Criddle, N. R., Taylor, M. J., and Pendleton, W. R.:
604 Coordinated investigation of mid-latitude upper mesospheric temperature inversion layers and
605 the associated gravity wave forcing in Logan, Utah, *J. Geophys. Res. Atmos.*, 119, 3756–3769,
606 <http://doi:10.1002/2013JD020586>, 2014.